MATER. RES. LETT.
2020, VOL. 8, NO. 7, 247–253
https://doi.org/10.1080/21663831.2020.1745920

MATERIALS RESEARCH LETTERS
Taylor & Francis
Taylor & Francis Group

ORIGINAL REPORT

Hierarchical {332} < 113 > twinning in a metastable β Ti-alloy showing tolerance to strain localization

Jinyong Zhang[a,b], Yangyang Fu[a], Yijin Wu[a], Bingnan Qian[c], Zheng Chen[a], Akihisa Inoue[a], Yuan Wu[d], Yang Yang[e], Fan Sun[c], Ju Li[e] and Frédéric Prima[c]

[a]School of Material Science and Engineering, China University of Mining and Technology, Xuzhou, People's Republic of China; [b]State Key Laboratory of Solidification Processing, Northwestern Polytechnical University, Xi'an, People's Republic of China; [c]PSL Research University, Chimie ParisTech-CNRS, Institut de Recherche de Chimie Paris, Paris, France; [d]State Key Laboratory for Advanced Metals and Materials, University of Science and Technology Beijing, Beijing, People's Republic of China; [e]Department of Nuclear Science and Engineering and Department of Materials Science and Engineering, Massachusetts Institute of Technology, Cambridge, MA, USA

ABSTRACT

A hierarchical {332} < 113 > twinning system is studied in a metastable beta Ti-12Mo-10Zr (wt%) alloy, which shows strong twinning-induced plasticity (TWIP) effect due to a three-level twinning mechanism. *In-situ* digital image correlation (DIC) indicates a good tolerance to strain localization until $\epsilon_{max} = 0.4$ thanks to TWIP hardening effect. The local shear misfit due to the intersection between the matrix slip bands and the primary twin boundaries is accommodated by the formation of secondary and tertiary sub-twinning structures. The strain accommodation postpones crack nucleation at the slip-twin intersections, contributing to the high tolerance of the strain localization.

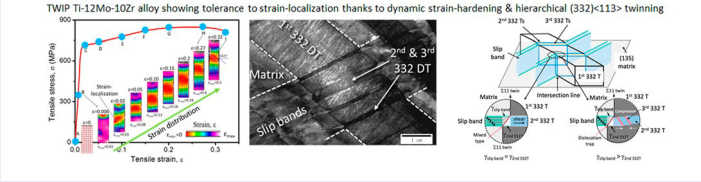

ARTICLE HISTORY
Received 18 January 2020

KEYWORDS
Beta TWIP Ti-alloy; hierarchical deformation twinning; tensile ductility

Impact Statement

The metastable Ti-12Mo-10Zr alloy displays a high tolerance to strain localization in tension thanks to the dynamic strain-hardening effect and local strain accommodation by the hierarchically self-organized triple {332} < 113 > deformation twinning.

Commercial Ti-alloys have been widely used in the fields of aerospace, biomedical, automotive and petrochemical industries. However, low strain-hardenability and insufficient damage tolerance are the two major weaknesses that limit the use of Ti-alloys when comparing to steels. Recently, new strategies inspired from TRIP (transformation-induced plasticity) and TWIP steels have been followed to overcome these weaknesses in β metastable Ti-alloys. In the last decade, by tuning the simultaneous or sequential activation of deformation modes among dislocation slips, deformed twins (DTs) and stress-induced martensitic transformation (SIMT), a new family of TRIP/TWIP β Ti-alloys [1–6] has been developed, exhibiting excellent combination of high strength, large ductility and improved strain-hardening rate. The relationships among the three deformation mechanism and their effects on mechanical performances in the TRIP/TWIP Ti-alloys have been studied in detail. Interestingly, some hierarchical substructures such as secondary SIMT and secondary/tertiary DTs are reported in TRIP/TWIP Ti-alloys as accommodation mechanisms [7,8]. Regarding the triple twinning structure, hierarchical lengthscales have been observed in pure titanium [9]. In the Ti-alloys dominated by single {332} < 113 > DT mode (hereafter termed as 332T), the occurrence of hierarchically self-organized structures

CONTACT Fan Sun fan.sun@chimieparistech.psl.eu PSL Research University, Chimie ParisTech-CNRS, Institut de Recherche de Chimie Paris, Paris 75005, France; Ju Li liju@mit.edu Department of Nuclear Science and Engineering and Department of Materials Science and Engineering, Massachusetts Institute of Technology, 77 Massachusetts Avenue, Cambridge, MA 02139, USA

Supplemental data for this article can be accessed here. https://doi.org/10.1080/21663831.2020.1745920

and their impact on mechanical properties become of great interest for TWIP Ti research. In this work, we report a study of hierarchical microstructure of a three-level deformation 332 T and the mechanism of its impact on the alloy's tolerance to strain localization. The TWIP Ti-alloy used in this study is a metastable beta Ti-12Mo-10Zr (wt%) alloy designed by 'd-electron' strategies [10]. The microstructural characterization of hierarchical structure was analysed by electron backscatter diffraction (EBSD) and transmission electron microscopy (TEM) techniques. The 2D full-field strain distribution was analysed by the *in-situ* optical digital image correlation (DIC) technique.

The cylindrical ingot of Ti-12Mo-10Zr (160 mm in diameter) was prepared by vacuum arc-melting under a high-purity Ar atmosphere using Ti-Mo master alloy and high purity Ti and Zr sponges. The processing of samples is the same as our previously reported method [1]. DIC technique with a camera recording was used during the tensile test. A 2D full-field strain map was recorded at a rate of 3 frames/second. The details of the technique can be found in reference [11]. The tensile test was conducted using an INSTRON 5967 machine at a constant strain rate of 10^{-3} s^{-1}. The strain maps were processed by Instron® DIC Replay Software. Phase characterization was carried out by X-ray diffraction (XRD) using Bruker D8 ADVANCE with Cu Kα radiation operating at 40 kV and 40 mA. Deformation microstructures were analysed by EBSD scans performed on a scanning electron microscope (SEM) operating at 20 kV. A JEOL 2100 microscope operating at 200 kV was used to carry out fine microstructural analysis.

Figure 1(a) displays the stress–strain curves of Ti-12Mo-10Zr and the DIC strain-distribution maps at different strain levels. The yield stress and ultimate tensile stress are about 730 and 1090 MPa, respectively, which represent much higher values than the Ti-12Mo strength reported elsewhere [1]. This can be attributed to the full suppression of SIMT and the solution strengthening effect provided by the zirconium addition [4]. A series of frames of the DIC video shows the 2D full-field strain maps at different strain levels (Figure 1(a)). It can be seen that a shear zone [12] (indicated in Figure 1(a)) occurs at the onset of plasticity ($\epsilon = 0.02$). With increasing tensile strain to $\epsilon = 0.05$, the shear zone spreads in width along the sample length. From $\epsilon = 0.05$ until fracture, the plastic zone stays at the same location, contributing to higher local tensile strain (ϵ_{max}) than overall ϵ. This phenomenon, according to Considère's criterion, usually leads to rapid decreasing stability with respect to necking in many BCC metals which lack sufficient strain-hardenability. Similarly, in the present alloy, the strain localization occurred at the very beginning of the plastic

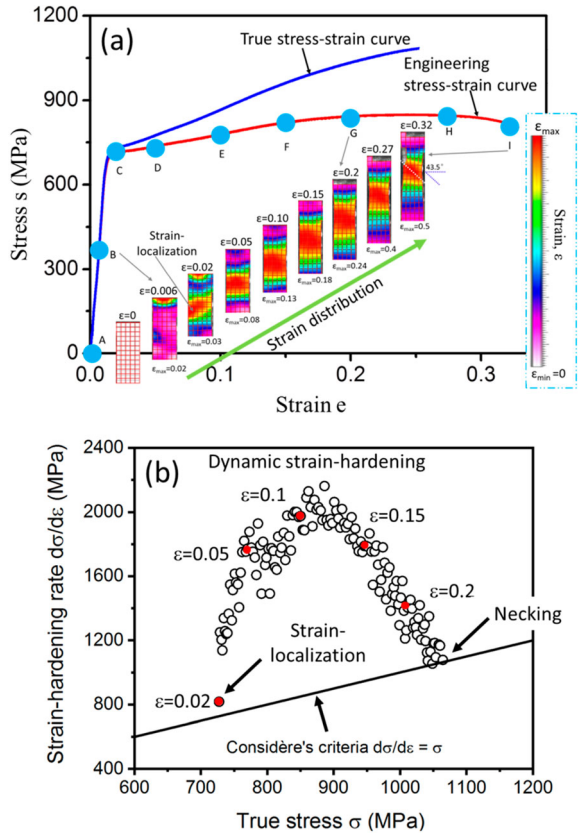

Figure 1. (a) Engineering strain-stress curve and true strain-stress curve of ST sample. The 2D full-field strain maps and the corresponding max of tensile strain (defined as ϵ_{max}) at different strain levels, as well as the bar of strain distribution, were also displayed in the inset of (a). The different strain levels were marked with the capital letter 'A ~ I' in (a), respectively; (b) Strain-hardening rate vs true stress. The Considère's criteria $d\sigma/d\epsilon = \sigma$ line was also plotted in (b).

regime (Figure 1(b), $\epsilon = 0.02$) due to the weak hardening rate (730 MPa) is almost equal to the yielding strength near Considère's criteria line. However, instead of necking, the stable plastic flow was immediately restored by the rapid increasing of hardening rate until $\epsilon = 0.12$, then maintained by the decreasing of the hardening rate to $\epsilon = 0.25$ ($\epsilon_{max} = 0.4$) before the hardening rate drops below the Considère's criteria line. The stabilized plastic flow suggests a dynamic strain-hardening mechanism of the alloy in addition to the conventional dislocation slip mechanism in BCC alloys. The initial structure of Ti-12Mo-10Zr is presented in Supplementary Figure 1.

Figure 2 shows EBSD analysis results concerning the deformation structure of Ti-12Mo-10Zr on a macro-scale. The grain boundaries are clearly visible in EBSD inverse pole figure (IPF) map (Figure 2(a)). The high density of parallel or interlaced deformation bands with different colour contrast are observed in each grain marked as Grain 1 ~ 5, suggesting that both fast multiplication

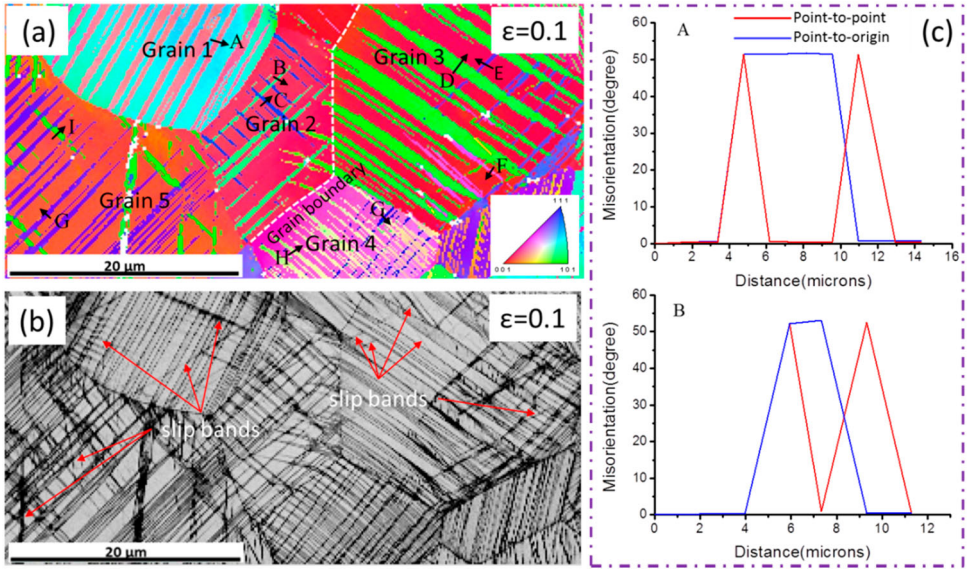

Figure 2. EBSD analysis of Ti-12Mo-10Zr sample at strain $\epsilon = 0.1$. (a) IPF map. The deformation bands were also symbolled by capital letters 'A ~ I' with arrows, respectively; (b) Image quality (IQ) maps. The traces of slip bands were also marked with red arrows; and (c) Misorientation profile along the arrows labelled A and B in (a) as typical examples.

and thickening of the deformation bands occurred with the continuous accumulation of strain. The crystallographic relationship between the bands and matrix are identified to correspond to $\{332\}<113>$ system. Two examples of the misorientation measurements are shown in Figure 2(c), the characteristic 50.5° (CSL Σ11) [13] is confirmed. The sizes of these 332Ts are in the range of a few micrometers. The activation of different 332T variants can be seen in some grains, depending on their orientation with respect to the external stress. It can be seen from image quality (IQ) maps (Figure 2(b)) that some slip bands intersect with the 332T bands. It is worth noting that no SIMT α' was observed in this alloy, consistently with XRD results shown in Supplementary Figure 1(b). The observed 332Ts are directly formed from the matrix, denoted as 'primary 332T' hereafter, intersecting the slip planes of the matrix, thus reducing the mean-free path of dislocation slip. The primary 332T can be also proved by TEM observation. Supplementary Figure 2 shows an overview of TEM images of primary 332T (1st 332T) and secondary 332T (2^{nd} 332T). According to the Hall-Petch effect, the primary 332T is a strain-hardening mechanism resulting from the dynamical reduction of dislocation mean free path during its multiplication. In addition to the efficient hardening effect due to the primary 332 T boundaries as dislocation slip barriers, accommodation mechanisms to relax strain localization and damage at these intersections are of great importance to postpone the premature crack nucleation.

Careful TEM investigations are performed on the 332 T and its interfaces. Interestingly, a tertiary $\{332\}<113>$ twin (3^{rd} 332 T) was identified in the 2^{nd} 332 T by TEM, where the 2^{nd} to 3^{rd} 332 T follows the same crystallographic orientation relationship as the 1^{st} to 2^{nd} 332 T system. Figure 3 shows TEM analysis of the hierarchical $\{332\}<113>$ twinning structures at multiple length scales. Figure 3(a) shows a primary deformation band (about 2 μm in width) with several secondary bands (about 100–300 nm in width). The secondary deformation bands and their internal tertiary bands were visible in the higher magnification TEM image, as shown in Figure 3(b). The above deformation bands are identified to be 332-type DT with habit plane parallel to the common twin 332 planes between parent and twin product, consistently with previous reports [1]. In this work, the TEM foil was tilted to [101] zone axes (ZA) of the primary deformation band, as the reference orientation. The orientation relation between the primary and secondary deformation bands (Figure 3(e)) is in agreement with the Σ11 coincidence site lattice of $\{332<113>$ twinning system [13]. By using the similar method, the secondary 332 T bands and tertiary 332 T bands were also identified by the corresponding selected-area electron diffraction (SAED) pattern (Figure 3(e–f)). However, as the matrix is a few degrees deviated from its [101] ZA, the corresponding SAED pattern of the matrix near $[3\bar{1}5]$ ZA is shown in Figure 3(c). By reconstructing the crystallographic projection, it is found that the primary twin plane is $(\bar{3}\bar{3}2)_{Matrix}$, which is not orientated at edge-on conditions in our characterization (about 10° inclined from beam axis). The same trace analysis method is also used to identify the possible planes of slip band contrast in the

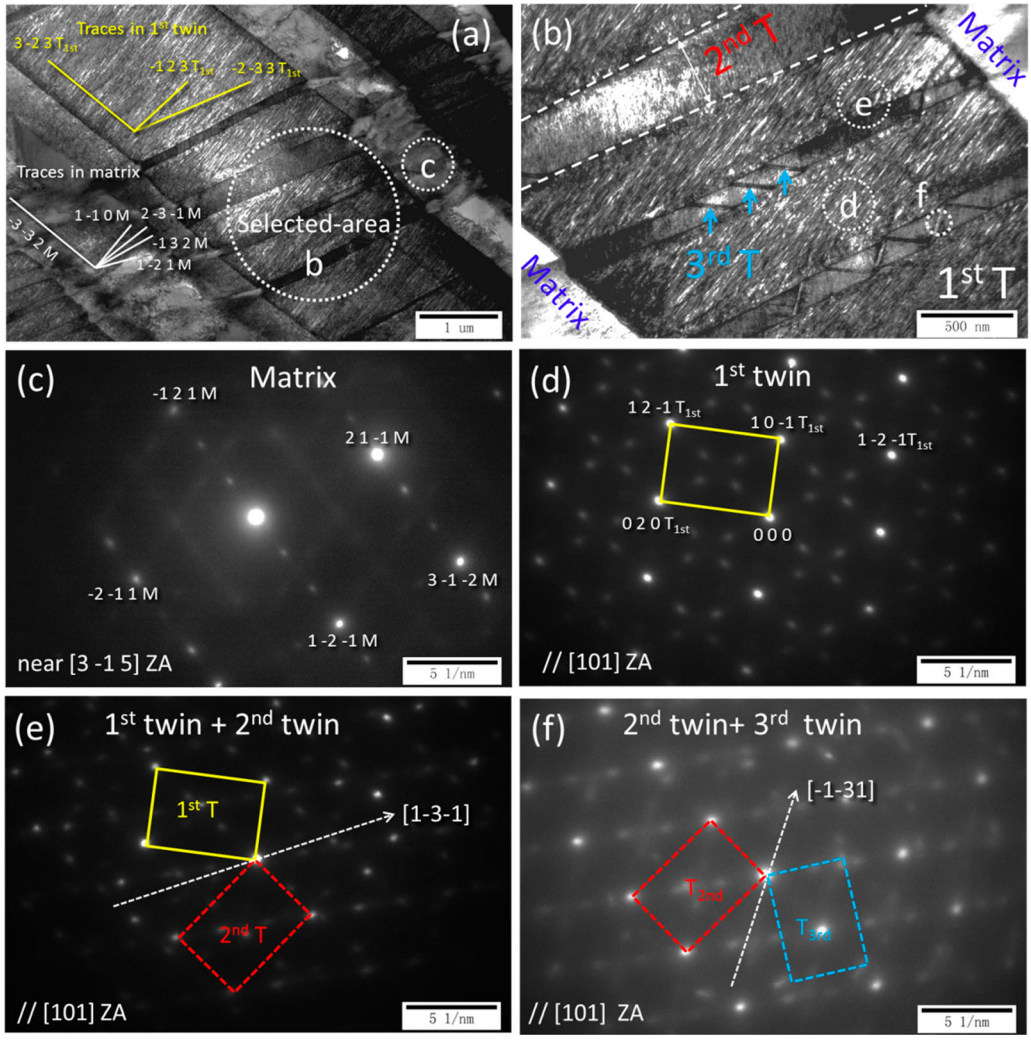

Figure 3. TEM images of the hierarchical structure of triple 332 T. (a) Bright-field image of triple 332 T (Lower magnification overview); (b) Close-up bright-field image of selected-area b in (a): matrix (M), primary 332 T, secondary 332 T and tertiary 332 T. The traces in the matrix and primary 332 T analysed by the trace method [14] were presented in (a). The selected-areas c, d, e and f were also highlighted by the dotted circle in (a) and (b); (c–f) SAED of selected-areas c, d, e and f, respectively. The zone axes (ZA) of the matrix is near $[3\bar{1}5]_{\beta}$, and the common ZA of $[101]_{\beta}$ is shared by primary, secondary and tertiary 332 T.

matrix. The three planes in coincidence are found to be $(1\bar{1}0)$, $(1\bar{2}\bar{1})$ and $(2\bar{3}1)$, which are the classic slip systems of BCC alloy. Among these 48 possible slip systems in bcc alloy, there are 24 {123} and 12 {112} with unique shear direction and 6 {110} in two directions. As observed in the deformed samples, traces of all three plane families can be seen when measuring the interface orientation of the slip bands, probably suggesting a cross-slip activity (lines marked in Figure 3(a)). Similar phenomena have been reported in reference [4]. Likewise, note that the bright-field contrast of the intersection interface between matrix and secondary 332 T was also observed in Figure 3(a), which could be regarded as cross-slip bands based on the slip trace analysis [14]. Such slips, including the screw dislocation slip and cross-slip bands, contribute essentially to the plastic flow of this alloy.

Based on the TEM imaging results, Figure 4 shows a schematic illustration of the 3D view and cross-section views concerning the formation sequence of primary 332 T (1st T), secondary 332 T (2^{nd} T) and tertiary 332 T (3^{rd} T). The 3D view is reproduced based on the TEM images (Figure 4(a–b)) by illustrating the 'hidden' planes in the foil thickness to understand the inter-plane geometries discussed. And the cross-section views are intended to explain the proposed mechanisms by showing relative positions of the planes and their notations used in this work. A coincidence is found between the incoming slip band $(\bar{1}32)[\bar{1}\bar{1}1]_{matrix}$ and the 2^{nd} 332 T, that they share the common intersection line (indicated in 3D view of Figure 4) on the 1st 332 T interface. The geometry measurements show that their habit planes are almost parallel, and the angle between the Burgers vector of the

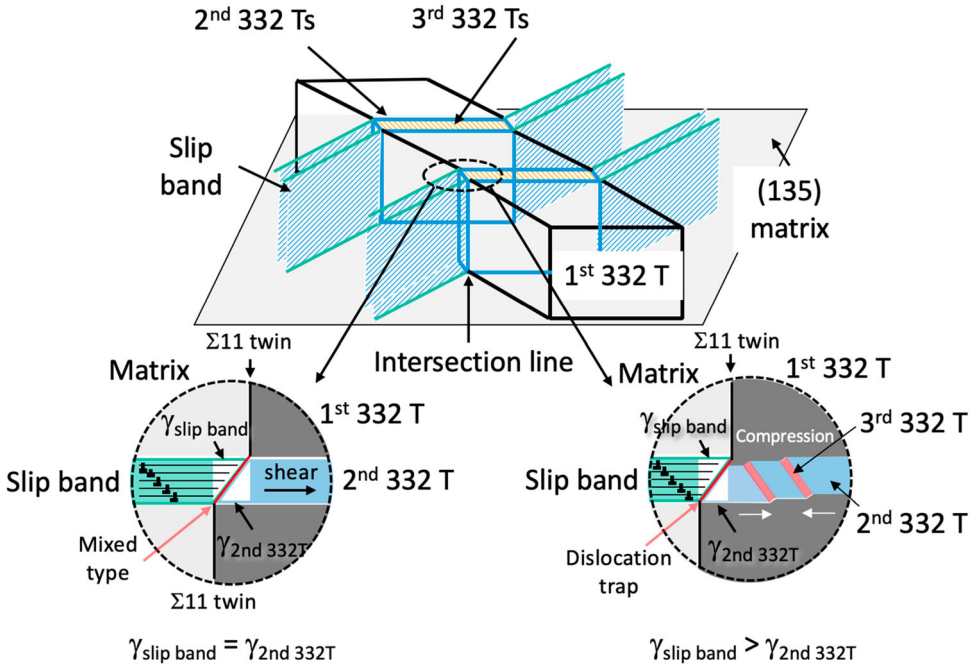

Figure 4. Schematic illustration of the 3D view and cross-sectional views concerning the formation sequence of primary 332 T, secondary 332 T and tertiary 332 T.

slip band (Burgers vector is a/2[$\bar{1}\bar{1}$1]) and the twinning direction is about 40°. The Geometric Criterion (GC) [15] can be used, as an index to be minimized as possible, to predict which slip or twinning system could be activated at an interface in response to an incoming slip band. The present GC index is about −0.77, which is one of the lowest values among all combinations of the slip and twinning systems on either side of the interface. Based on this finding, it is presently thought that the localized shear strain due to dislocation pile-up at the 1st 332 T boundary may be accommodated by the formation of an appropriate 2nd 332 T variant. Some details of the accommodation process can be discussed with regard to the slip-interface interaction [16]. Here, the 332 T interface can be characterized as Σ11 (332) boundaries, which act as effective obstacles for slip transfer, leading to dislocation pile-up at the left-hand side of the interface [15]. Stress concentrations consequently happen at both sides of the interface close to the pile-up site. On the right-hand side, the stress concentration points act as sources of new dislocation slips or twinning operations to accommodate the slip strain [17]. In the present case, the 2nd 332 T bands are formed to relax the stress concentration. At the intersection between slip band and 332 T, it can be observed that the interface orientation is tilted from the original 332 T orientation (observed in Figure 3(a–b) and illustrated in Figure 4), which demonstrates the magnitude of shear deformation. A perfect shear compatibility can be established when the total shear strain 'γ_{slipband}' induced by slip band equals to the shear strain 'γ_{2nd332T}' provided by the thickening of the 2nd 332 T band (Figure 4). However, the balance is about to break when 'γ_{slipband}' continues to increase locally in the slip band along with the plastic flow.

It should be pointed out that the 2nd twinning operation has changed interface structure at the intersection (from Σ11 to mixed type, indicated in Figure 4). The change of the interface structure associates with the change of slip-interface interaction [16,18]. One pair of slip systems, $(\bar{1}32)[\bar{1}\bar{1}1]_{\text{matrix}}$ and $(\bar{2}3\bar{1})[111]_{\text{2nd332T}}$, is found likely to fulfill the direct slip transfer criterion. The Geometric Criterion index is about −0.8, the lowest among all combinations. However, the direct slip transfer usually involves a trapping process of the incoming dislocation at interface, leading again to stress accumulation [17,19]. Previous experimental study has shown that a high resolved shear stress, about 2 times higher than the yielding stress, is required to push the dislocation out of the boundary [18]. In TWIP Ti-alloys, such stress level is largely sufficient to activate 332 T. As a matter of fact, the 3rd twinning structures are indeed observed in most of the 2nd twin bands (Figure 3). Therefore, it would be reasonable to suggest that when 'γ_{slipband}' > 'γ_{2nd332T}', a compressive stress is likely accumulated in the 2nd 332 T along the slip transfer direction, resulting in the formation of the 3rd 332 T as a supplementary accommodation mechanism.

Some discussions can be addressed to the relation between the hardening mechanism by 1st 332 T and the accommodation mechanism. The synergetic co-operation of these two mechanisms is thought to be one of the reasons for the macroscopic tolerance to strain localization. Analogous to the Ti-alloys operating in TWIP/TRIP [1,5], similar synergy may exist between twinning and martensitic transformation, which play roles for strain-hardening and for strain misfit accommodation, respectively. As a result, these alloys also present very stable plastic flow accompanied by strong strain hardening effect. Furthermore, the activation of the 1st deformation mechanism is determined by the chemical stability of β phase. The activation sequence has been reported to be SIMT-332T-112T when increasing the β stability. It is assumed that the stability of solution-treated Ti-12Mo-10Zr should be situated between Ti-12Mo and Ti-13Mo-18Zr, because the 1st deformation mechanism of Ti-12Mo is TRIP + TWIP 332T [1,20] and the Ti-13Mo-18Zr is TWIP 332T+112T mode [4]. Similarly in the selection of $2^{nd}/3^{rd}$ accommodation mechanisms, the Ti-12Mo presents 2^{nd} martensite and $2^{nd}/3^{rd}$ 112T in the 1st 332T, whereas the TWIP Ti-13Mo-18Zr presents low volume fraction of 2^{nd} 332 twinning and the formation of a special {5 8 11} twinning [4]. Comparing to the triple 332T observed in the Ti-12Mo-10Zr, these differences might suggest that the selection of 2^{nd} and 3^{rd} accommodation mechanisms is also affected by the β chemical stability.

The hierarchical structures of primary, secondary and tertiary 332T, at multiple length scales, construct a 'composite band' [1] under the uniaxial tensile load in Ti-12Mo-10Zr. The 332T bands have been proved to contribute to the strain hardening effect in TWIP Ti-alloys, which probably results from both the dynamic reduction of the mean free path for dislocation glide by the growing twinning network [2,4] and the mechanical contrast effect of the twins/matrix [4]. The shear strain concentration starting at a strain of 0.02 until 0.32 suggests that intensive dislocation slip and 332T happened in the same volume of the sample all along the tensile deformation to fracture. The 332T interface intersects the dislocation slip along (110), (112) or (123) planes as effective barriers, leading to intense stress concentration at the twin/matrix interfaces. In the absence of an efficient accommodation mechanism, such concentration will lead to damage and early nucleation of cracks at the twins/matrix interfaces. The proposed accommodation mechanism in Ti-12Mo-10Zr is a hierarchical sub-twinning mechanism to maintain the plastic flow strain up to $\epsilon_{max} = 0.5$ before fracture. The strain-hardening effect reflects the incremental dislocation density, which associates to the slip-twin interaction and the simultaneous augmentation of 1st 332T density. The hierarchical 332T twinning shows an auto-accommodated microstructure at each twinning level. It suggests that this hierarchical twinning mechanism can be comparable to the hierarchical microstructure reported in TRIP/TWIP Ti-Mo and Ti-V-Cr-Al alloy, in which 2^{nd} martensite formed in the 1st 332T plays the role of accommodation to the local strain misfit [1,5]. In another Ti-Mo-Zr alloy with higher Zr content (Ti-13Mo-18Zr), this hierarchical twinning mechanism has also been observed as one of the accommodation mechanisms in addition to the {5 8 11}-type twinning at 332T boundaries [4]. These facts suggest that the activation of the hierarchical 332T could probably be dependent to alloy chemical composition. Owing to the hierarchical twinning accommodation, the Ti-12Mo-10Zr presents high tolerance to localized stress concentration.

Disclosure statement

No potential conflict of interest was reported by the author(s).

Funding

The work was supported by the National Natural Science Foundation of China (grant numbers 51601216 and 51771226); China Postdoctoral Science Foundation (grant number 2018M632414); Fund of State Key Laboratory for Mechanical Behavior of Materials, Xi'an Jiaotong University (grant number 20182008); Fund of State Key Lab of Advanced Metals and Materials, University of Science and Technology Beijing (grant number 2019-ZD03); Funds of Industry-University-Research Cooperation in Jiangsu Province (grant number BY2018075) and Fund of Graduate Education and Teaching Reform of CUMT (grant number 2019YJSJG061).

References

[1] Sun F, Zhang JY, Marteleur M, et al. Investigation of early stage deformation mechanisms in a metastable β titanium alloy showing combined twinning-induced plasticity and transformation-induced plasticity effects. Acta Mater. 2013;61(17):6406–6417.

[2] Min X, Chen X, Emura S, et al. Mechanism of twinning-induced plasticity in β-type Ti–15Mo alloy. Scr Mater. 2013;69(5):393–396.

[3] Lai MJ, Tasan CC, Raabe D. On the mechanism of {332} twinning in metastable β titanium alloys. Acta Mater. 2016;111:173–186.

[4] Zhang J, Sun F, Chen Z, et al. Strong and ductile beta Ti–18Zr–13Mo alloy with multimodal twinning. Mater Res Lett. 2019;7(6):251–257.

[5] Lilensten L, Danard Y, Brozek C, et al. On the heterogeneous nature of deformation in a strain-transformable beta metastable Ti-V-Cr-Al alloy. Acta Mater. 2019;162:268–276.

[6] Zhang J, Li J, Chen G, et al. Fabrication and characterization of a novel β metastable Ti-Mo-Zr alloy with large ductility and improved yield strength. Mater Charact. 2018;30/03(139):421–427.

[7] Mantri SA, Sun F, Choudhuri D, et al. Deformation induced hierarchical twinning coupled with omega transformation in a metastable beta-Ti alloy. Sci Rep. 2019;9(1):1334.
[8] Qin H, Jonas JJ. Variant selection during secondary and tertiary twinning in pure titanium. Acta Mater. 2014;75:198–211.
[9] Sun F, Zhang JY, Vermaut P, et al. Strengthening strategy for a ductile metastable β-titanium alloy using low-temperature aging. Mater Res Lett. 2017;5:547–553.
[10] Morinaga M, Yukawa N, Maya T, et al. Theoretical design of titanium alloys. Sixth World Conference on Titanium. III; 1988; Cannes; France; 6–9 June 1988.
[11] Kavdir EÇ, Aydin MD. The investigation of mechanical properties of a structural adhesive via digital image correlation (DIC) technic. Compos Part B: Eng. 2019;173:106995.
[12] Yuan F, Yan D, Sun J, et al. Ductility by shear band delocalization in the nano-layer of gradient structure. Mater Res Lett. 2018;7(1):12–17.
[13] Ranganathan S. On the geometry of coincidence-site lattices. Acta Crystall. 2010;21(2):197–199.
[14] Marichal C, Van Swygenhoven H, Van Petegem S, et al. {110} Slip with {112} slip traces in bcc Tungsten. Sci Rep. 2013;3:2547.
[15] Kacher J, Eftink BP, Cui B, et al. Dislocation interactions with grain boundaries. Curr Opin Solid St M. 2014;18(4):227–243.
[16] Sutton AP, Balluffi RW. Interfaces in crystalline materials. London: Oxford University Press; 1995.
[17] Kacher J, Robertson I. Quasi-four-dimensional analysis of dislocation interactions with grain boundaries in 304 stainless steel. Acta Mater. 2012;60(19):6657–6672.
[18] Poulat S, Decamps B, Priester L. Weak-beam transmission electron microscopy study of dislocation accommodation processes in nickel $\Sigma = 3$ grain boundaries. Philos Mag A. 1998;77(6):1381–1397.
[19] Polcarová M, Gemperlová J, Jacques A, et al. Synchrotron radiation topographic study of slip transfer across grain boundaries in Fe–Si bicrystals. J Phys D: Appl Phys. 2006;39(20):4440.
[20] Zhang JY, Li JS, Chen Z, et al. Microstructural evolution of a ductile metastable β titanium alloy with combined TRIP/TWIP effects. J Alloy Compd. 2017;3/30(699):775–782.

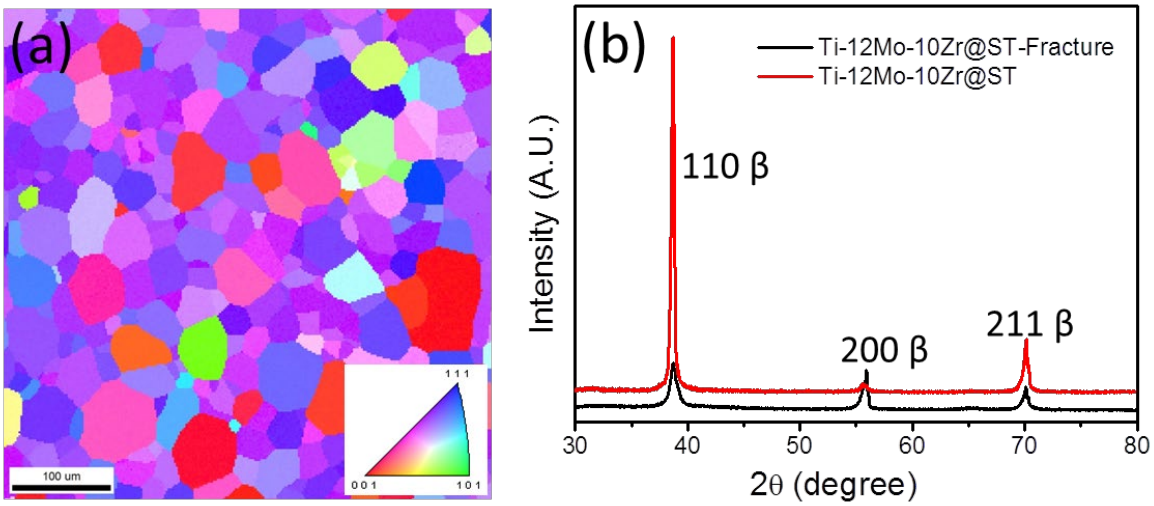

Supplementary Figure 1. (a) EBSD IPF map of ST sample; (b) XRD profiles of ST sample and subsequent fractured sample.

It can be seen that equiaxial β grains with grain size of several tens of microns are observed by EBSD mapping at as-quenched state. The XRD patterns confirm the presence of β phase before tensile test. Deformation induced martensite was not detected in the fractured sample, indicating the absence of SIMT and TRIP effect (further confirmed by EBSD and TEM results). The presence of athermal ω is not detected by XRD due to the nanometric size of these precipitates, and thereafter confirmed by TEM characterization.

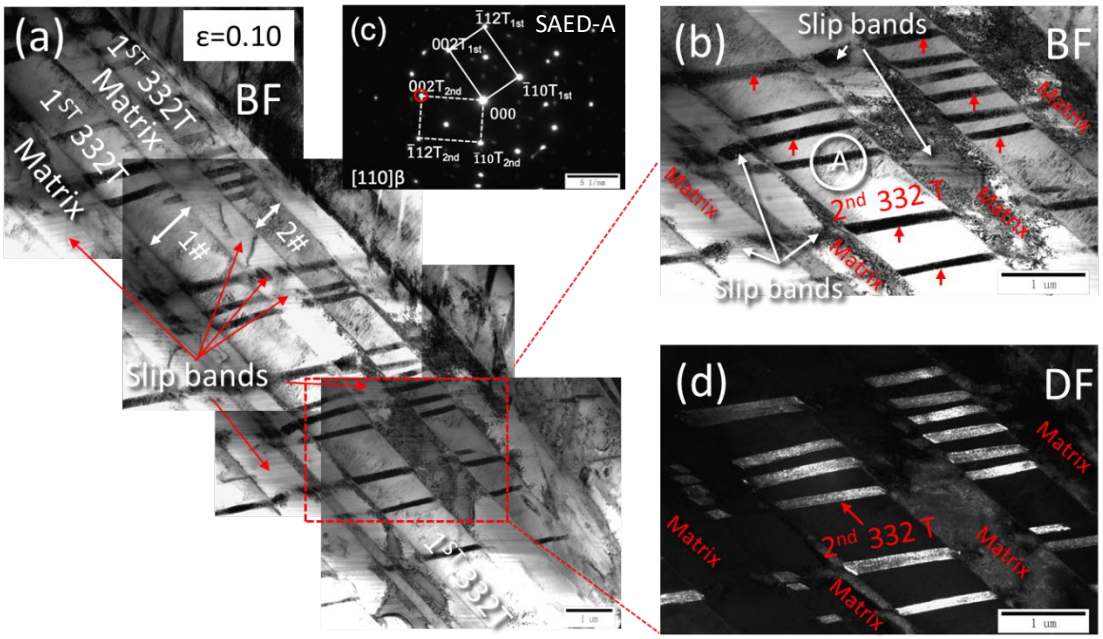

Supplementary Figure 2. TEM images of primary 332T (1st 332T) and secondary 332T (2nd 332T). (a) Bright-field image of primary deformation bands, which can be identified as {332}<113> twinning system through the selected-area electron diffraction (SAED) pattern. They are called as "primary 332T bands". Two primary 332T bands were also labelled as 1# and 2# bands, respectively; (b) Bright-field image of a selected area in (a), showing a set of parallel bands (marked by red arrow) inside the 1st 332T bands. A selected area is also marked by a white circle with capital letter 'A' in (b). These parallel bands can be identified as the secondary 332T bands (2nd 332T) by corresponding SAED-A pattern; (c) The corresponding SAED-A pattern along [110]β zone axis; and (d) Dark-field image of secondary 332T using marked diffraction spot (the red circle) in (c). Moreover, the slip bands marked by the arrows in (a) and (b) are also observed intersecting the primary 332Ts, showing a weak contrast on the bright field image.